Range verification for eye proton therapy based on proton-induced x-ray emissions from implanted metal markers

2014 Phys. Med. Biol. 59 2623

(http://iopscience.iop.org/0031-9155/59/11/2623)

OPEN ACCESS
IOP Publishing | Institute of Physics and Engineering in Medicine Physics in Medicine and Biology

Phys. Med. Biol. **59** (2014) 2623–2638 doi:10.1088/0031-9155/59/11/2623

Range verification for eye proton therapy based on proton-induced x-ray emissions from implanted metal markers

Vanessa La Rosa[1], **Andrzej Kacperek**[2], **Gary Royle**[1] **and Adam Gibson**[1]

[1] Department of Medical Physics and Bioengineering, University College London, WC1E 6BT, UK
[2] Douglas Cyclotron, Clatterbridge Cancer Centre NHS Foundation Trust, Bebington, Wirral, CH63 4JT, UK

E-mail: larosa@detector-med.com

Received 29 November 2013, revised 15 February 2014
Accepted for publication 3 March 2014
Published 1 May 2014

Abstract

Metal fiducial markers are often implanted on the back of the eye before proton therapy to improve target localization and reduce patient setup errors. We aim to detect characteristic x-ray emissions from metal targets during proton therapy to verify the treatment range accuracy. Initially gold was chosen for its biocompatibility properties. Proton-induced x-ray emissions (PIXE) from a 15 mm diameter gold marker were detected at different penetration depths of a 59 MeV proton beam at the CATANA proton facility at INFN-LNS (Italy). The Monte Carlo code Geant4 was used to reproduce the experiment and to investigate the effect of different size markers, materials, and the response to both mono-energetic and fully modulated beams. The intensity of the emitted x-rays decreases with decreasing proton energy and thus decreases with depth. If we assume the range to be the depth at which the dose is reduced to 10% of its maximum value and we define the residual range as the distance between the marker and the range of the beam, then the minimum residual range which can be detected with 95% confidence level is the depth at which the PIXE peak is equal to 1.96 σ_{bkg}, which is the standard variation of the background noise. With our system and experimental setup this value is 3 mm, when 20 GyE are delivered to a gold marker of 15 mm diameter. Results from silver are more promising. Even when a 5 mm diameter silver marker is placed at a depth equal to the range, the PIXE peak is 2.1 σ_{bkg}. Although these quantitative

results are dependent on the experimental setup used in this research study, they demonstrate that the real-time analysis of the PIXE emitted by fiducial metal markers can be used to derive beam range. Further analysis are needed to demonstrate the feasibility of the technique in a clinical setup.

Keywords: proton-therapy, range, markers, eye, PIXE

(Some figures may appear in colour only in the online journal)

1. Introduction

Proton beams are particularly effective in cancer treatment because their dose rises sharply at the end of their penetration range (the Bragg peak) and quickly falls to zero beyond the range; this 'inverse depth-dose profile' allows radiation dose to distal critical healthy tissue to be minimized and was first recognized as being potentially useful for cancer therapy by Wilson (1946).

Since protons deposit their dose in a relatively small volume and their range is highly sensitive to variation and uncertainties in density and proton stopping power along the path of the beam, it is critically important to minimize all sources of uncertainty including all setup and organ motion. While uncertainties in the estimation of the margins in photon therapy might cause some under-dosage of the tumour, in proton therapy such an underestimation may mean that part of the tumour would receive an extremely low dose due to a potential shift in the sharp distal fall off (Paganetti 2012); on the other hand an overestimation could damage an organ at risk beyond the tumour (Smeets *et al* 2012).

Range is commonly defined as the position where dose has decreased to 90% of its maximum value beyond the Bragg peak. For a mono-energetic beam the 90% fall-off position is the mean projected range of a proton (i.e. the range at which 50% of proton fluence has decreased) (Berger 1993).

Rather than trying to minimize the range uncertainty, methods are being developed which aim to measure the range *in vivo*. The most frequently used method is positron emission tomography (PET) imaging. This technique images the activation of the patient's tissue by the proton beam and in particular positron emission due to reactions between protons and nuclei of ^{11}C, ^{13}N and ^{15}O (Parodi and Enghardt 2000).

A further method for *in vivo* range verification is to measure prompt gamma (PG) emission. This occurs after nuclear excitation by the proton beam in tissue (Polf *et al* 2009). However, even though this method gives a higher count rate and predicts the location of the Bragg peak more accurately than PET could do, it is not routinely used due to lack of detectors with sufficient efficiency.

Detectors (silicon diodes) placed inside human bodies have also been suggested (Lu 2008), yielding an accuracy in the estimation of the water-equivalent path length better than ± 0.5 mm at low doses (<0.5 cGy).

In this work we are interested in range verification during ocular treatments. The key importance is to obtain a good local control on the tumour while sparing the optical nerve and preserving the functionality of the eye (Kacperek 2009). A large number of proton treatments of uveal melanoma, the most common ocular tumour, achieved a local control rate of about 95% (Hocht *et al* 2004). It is located most frequently in the posterior part of the eye. A commonly used localization procedure for this kind of tumour involves the surgical application of four tantalum clips (2.5 mm diameter, 0.2 mm thickness) around the perimeter

of the tumour on the outer sclera (Munzenrider 1999). Precise patient alignment with the beam is then accomplished by means of x-ray imaging of those markers (Shin *et al* 2012). Eye axial length and height are estimated during the treatment planning phase by ultrasound with an uncertainty of 0.1–0.2 mm. Another source of uncertainty is provided by the range measurement, which is routinely performed in water as part of the QA procedures and is affected by an error of 0.2–0.3 mm. Range safety margins of 2–2.5 mm are usually applied but *in vivo* range verification is not routinely performed (Kacperek 2012).

We investigated the feasibility of implementing a tool for the real-time proton beam range verification for eye proton therapy and in particular for uveal melanoma. This involves surgically implanting a gold marker in the back of the eye between the tumour and the optic nerve in order to detect the proton-induced x-ray emissions (PIXE) generated by the interaction of the therapeutic proton beam with the target.

PIXE is a well-established non-destructive analytical technique in x-ray emission spectroscopy, which is typically used for rapid multi-element non-destructive analysis in a wide range of areas such as atmospheric science, geology, art and archaeology. Recently its efficacy in enhancing proton dose in mice has been proved by Kim *et al* (2010). However this is the first time its use is proposed for *in vivo* range verification in proton therapy.

In this paper we report a feasibility study, which is based on both experimental and simulated results, on the use of PIXE for range verification in eye proton therapy. In particular a gold and a silver marker are moved along the dose deposition curve of a typical mono-energetic (59 MeV) proton beam and a fully modulated beam, respectively. The detected characteristic x-rays from both metals are recorded at each depth. The aim is to assess whether if a measurable signal is still produced in the fall-off region of the Bragg peak (and spread out Bragg peak or SOBP) and determine the minimum detectable overshoot in a clinical situation. The limitations of the technique are described with possible solutions suggested for future developments.

2. Materials and methods

2.1. Principle of the approach

The intensity of detected characteristic x-rays (Y) generated by the interactions of protons with the atoms of a target during PIXE, is determined by equation (1) (Katsanos *et al* 1988):

$$Y = \Phi A f \int_{\text{surface}}^{R} \sigma(E)\, \mathrm{e}^{-\mu x}\, \mathrm{d}x \tag{1}$$

where Φ is the number of protons hitting the metal, A is the number of metal atoms per unit volume, f is a factor including corrections for the geometry, detector efficiency and external x-ray absorption, $\sigma(E)$ is the x-ray production cross-section for proton energy E, μ is the self-attenuation experienced by the produced x-rays in the metal, x is the depth in the metal at which the photons are generated and R is the proton range inside the metal target.

By placing a metal marker at the tumour base, near the optic nerve prior to an ocular proton treatment, we assume that if the range estimation is correct, the protons should stop before reaching the marker. In this case no PIXE would be detected and there would not be any dose deposited to the optic nerve. However, if the range is not correctly estimated, protons may travel beyond the tumour, interact with the marker, inducing x-ray emissions that could be detected and used to estimate the range inaccuracy. We define the residual range as the distance travelled by the protons beyond the marker. If we assume the range (R_0) to be the depth at

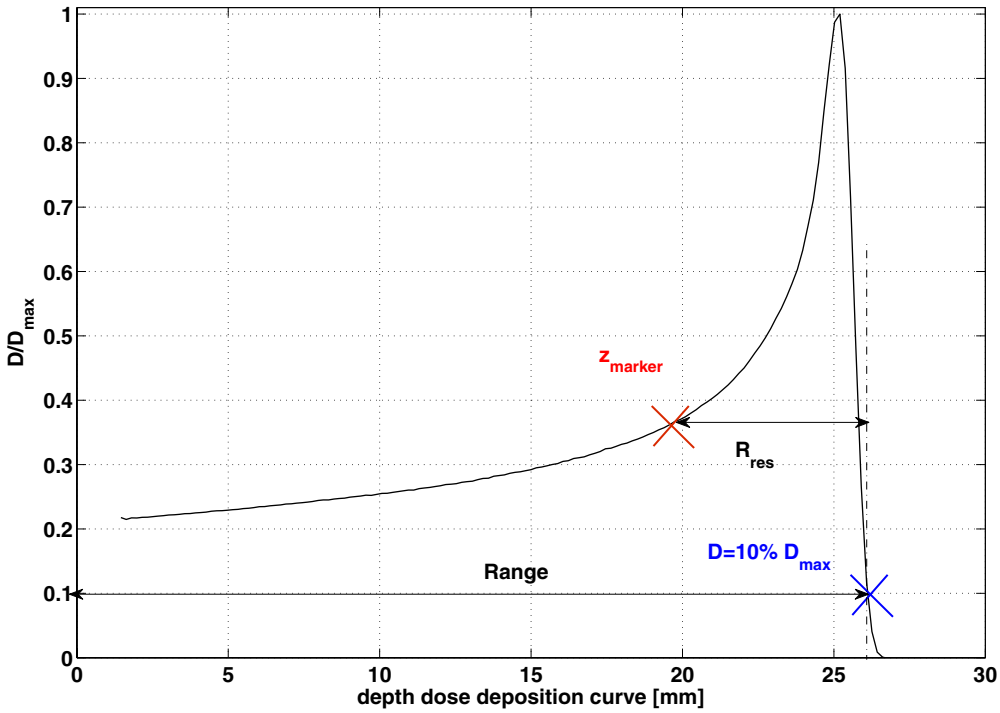

Figure 1. Residual range (R_{res}) definition. For our purposes we define the residual range as the path travelled by the protons beyond the marker position (z_{marker}). We assume the range (R_0) to be the position at which the absorbed dose beyond the Bragg peak or SOBP (D) falls to 10% of its maximum value (D_{max}).

which the dose is reduced by 90%, the residual range (R_{res}) can be calculated as the difference between the proton range and the depth of the marker z_{marker}, equation (2) (IAEA 2006):

$$R_{res} = R_0 - z_{marker} \tag{2}$$

as described in figure 1.

2.2. Experimental design

All measurements were made at the passive proton beam line CATANA, Catania (Italy). The experimental apparatus is shown in figure 2 and consists of a collimated CdTe detector (see section 2.5). The marker was placed at the treatment isocentre situated 10 cm axially from the nozzle. The nozzle collimator was made of brass and had a diameter of 15 mm. The x-ray emissions from brass are mainly due to Cu and Zn (in the range 8–10 keV). The CdTe detector was placed at 45° to the incident beam and to the marker and encased in a purpose built aluminium box with a lead collimator of 5 mm diameter to reduce the noise from low energy x-rays. Initial experiments and modelling showed that this was the optimal position to reduce the background signal due to neutrons and gamma emissions coming from the nozzle and increase the signal-to-noise ratio (SNR). The low energy gamma emissions were further reduced by shielding the detector with a 3 cm thick lead block. This thickness was chosen according to the results given by simulation as a good trade-off between background reduction and detector positioning.

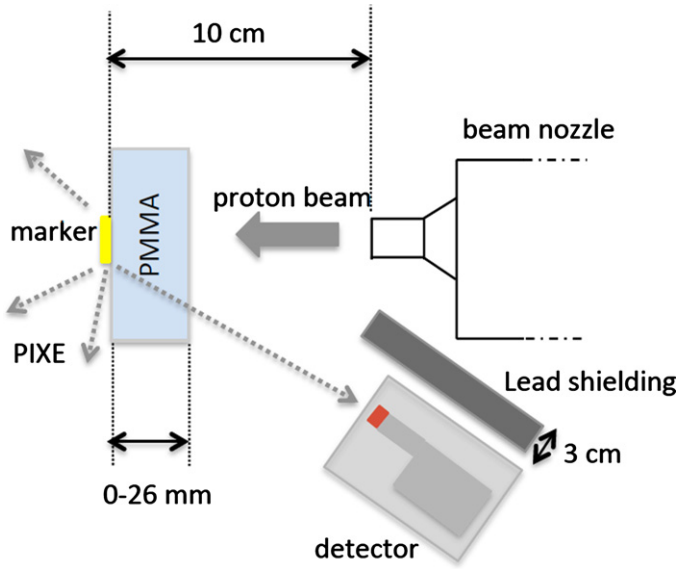

Figure 2. Experimental design. The marker was placed at the treatment isocentre situated 10 cm axially from the nozzle. PMMA slabs of increasing thickness were used to move the marker along the proton dose deposition curve. The CdTe detector was at 45° to the incident beam and to the marker and encased in a purpose built aluminium box. A 3 cm thick lead block reduced the low energy gamma emissions coming from the nozzle.

2.3. Proton beam line

Since this research study is focused on eye proton therapy, an eye proton therapy beam line was chosen, providing a maximum proton energy at the treatment isocentre of 59 MeV. The full width at half maximum (FWHM) of the Bragg peak is 2.76 mm. The 90%–10% and 80%–20% distal fall-offs are 0.8 and 0.6 mm, respectively, and the peak to entrance ratio is 4.72 (Cirrone *et al* 2004).

The CATANA beamline has been entirely built at the *Istituto Nazionale di Fisica Nucleare-Laboratori Nazionali del Sud* (INFN-LNS) of Catania. The proton beam exits the cyclotron through a 50 μm kapton (a polyimide film) window placed at about 3 m from the isocentre. Just before the exit window the first scattering foil made of 15 μm tantalum is placed in vacuum. The first element of the beam in air is a second tantalum foil 25 μm thick provided with a central brass stopper of 4 mm in diameter. The double foils scattering system is optimized to obtain a good homogeneity in terms of lateral off-axis dose distribution (Cuttone *et al* 2011).

2.4. Metal marker

The choice of the metal was made according to the following criteria:

- Biocompatibility: implantable markers need to be biocompatible and non-toxic.
- Characteristic peaks energy: sufficiently energetic x-rays are required in order for them not to be completely absorbed by the eye and be detected.
- SNR: metals with higher ionization cross-sections ensure high PIXE count rate. This enhances sensitivity and reduces counting time.
- Dose to tissues: dose due to secondary emissions needs to be kept as low as possible.

The preliminary investigations of this research were performed on a gold marker whose biocompatibility properties are well known. However due to its high atomic number, gold

has a lower ionization cross-section than lower atomic number metals like tantalum, silver or titanium (Paul and Sacher 1989). For 3 MeV protons, for instance, it has a cross-section of 1.85×10^{-2} barn, while the cross-sections for tantalum, silver and titanium are 4.14×10^{-2}, 2.60 and 4.40×10^{2} barn respectively. Titanium characteristic x-rays (4.5–5 keV) would be completely absorbed by the eye. Tantalum markers are sutured to the eye sclera prior to proton treatments for radiographic patient positioning. Since the signal intensities from clips of the same material would add up in the PIXE peak, tantalum was not further considered. However, preliminary studies were made on tantalum in order to ensure that the characteristic x-rays of the chosen metal would have been distinguishable from the signal emitted by currently implanted markers. Hence investigations were continued using a silver marker.

The markers used in this study had the thickness of the clinical implanted tantalum markers, that is 0.2 mm. A diameter of 15 mm was chosen for the gold marker in order to increase the signal intensity. A diameter of 5 mm was chosen instead for the silver marker which is closer to the size of the tantalum markers used clinically (3 mm diameter). The signal intensity will scale with the area of the marker, so we expect to obtain a signal which is 25 times higher for the gold marker and 2.77 times higher for the silver marker than we would obtain with a 3 mm marker.

2.5. Detector

A small and portable detector is needed for this application to be used in a clinical environment without interfering with the patient positioning. For the same reason detectors which require nitrogen cooling (such as HPGe x-ray detectors) are not suitable for this application.

We chose to use a CdTe detector (XR-100T, Amptek Inc., MA, USA). The primary advantage of CdTe with respect to Si detectors is its much greater efficiency, since the photoelectric cross-section scales as Z^5. Therefore while the efficiency of most Si detectors begins to fall above 10 keV, for 1 mm CdTe, the efficiency is maximum from 10 to 50 keV. It decreases at lower energies being around 5% lower from 10 down to 8 keV and 50% of its maximum value around 4 keV. At energies >50 keV it starts decreasing, being 92.20% at the gold K_{α_1} energy (68.8 keV) down to 63% of its maximum value at 100 keV (Redus 2010).

The detector consisted of a single planar CdTe crystal of diameter 5 mm with an active depth of 0.75 mm mounted on a thermoelectric Peltier cooler along with the input FET and critical feedback components (Redus *et al* 2006). A 100 μm beryllium window is placed in front of the detector. The digital processors include a multichannel analyser, the command and control interface and the bias voltage for the detector (500 V) (Redus *et al* 2009). The energy resolution of the CdTe detector was measured to be consistently less than 0.9 at 59.5 keV using an Americium-241 source.

The preamplified signals were processed by the Amptek's digital processor PX5 using trapezoidal shaping and no risetime discrimination. Data were acquired by the DPPMCA software provided by Amptek (2013).

Preliminary tests showed a shaping time of 2.4 μs to be a good compromise between energy resolution and pulse pile-up occurrence (and thus dead-time). This value was chosen for the whole measurement.

2.6. Measurement procedure

2.6.1. Range verification of a mono-energetic beam with a gold marker. The aim of this experiment is to correlate the number of detected characteristic photons with the residual range in tissue of a mono-energetic proton beam. A 15 mm diameter gold marker was moved

Table 1. Thicknesses of PMMA and corresponding proton energies for each of the 13 positions of the gold marker along the pristine Bragg peak curve.

PMMA thickness (mm)	Proton energy (MeV)
0	59
2.40	55.90
7.66	48.47
12.70	40.86
17.76	30.94
21.16	22.85
22.45	19.08
23.49	15.54
24.53	11.18
25.03	8.48
25.28	6.82
25.53	4.75
25.65	3.39

along the dose depth deposition curve. This was done by adding poly-methyl methacrylate (PMMA) slabs of increasing thickness, to produce the energies given in table 1. These energies were calculated for each thickness using the code provided by Meroli (2012), so that at each position of the marker, the residual range in tissue can be estimated and correlated with the number of detected counts.

A plane-parallel advanced Markus Ionization Chamber (type 34 045, PTW, Freiburg, Germany) was used as a reference of the dose depth deposition curve. The equivalent dose to tissue to the marker at each position was 20 GyE.

The lowest possible beam current of 0.7 nA (dose rate equal to 1 Gy min^{-1}) was used in order to reduce the count rate and the risk of pile-up in the amplifier.

The experiment was first simulated using the Monte Carlo software Geant4 (Agostinelli *et al* 2003), by using the model of CATANA beamline implemented by Cirrone *et al* (2009), as discussed in section 2.7. This provided us with a benchmark of our system and informed the experimental design.

2.6.2. Silver marker and SOBP. We tested the silver marker at different depths of a the SOBP. The nozzle collimator diameter was 15 mm and the dose at the plateau was 15 GyE, delivered at a dose rate of 12 GyE min^{-1}, all clinically realistic values. This increased the pile-up probability, but made the experiment more realistic. The SOBP pattern is composed of a weighted superposition of pristine *Bragg peaks* at different energies in order to deliver the same dose to the whole tumour volume in all its depth (Bortfeld and Schlegel 1999).

2.7. Monte Carlo simulation

During the preliminary phase of this research study Monte Carlo models were used to assess the feasibility of the technique, plan the experimental setup, design the shielding for the CdTe detector (mostly from high energy gamma emissions) and decide the best position for the detector with respect to the beamline. During the data processing phase they were useful in validating the experimental results, testing the reproducibility of the technique and estimating the outcome from different possible scenarios (e.g. changing the metal, the size of the marker or the relative position), without reproducing the experiment in a clinical treatment room.

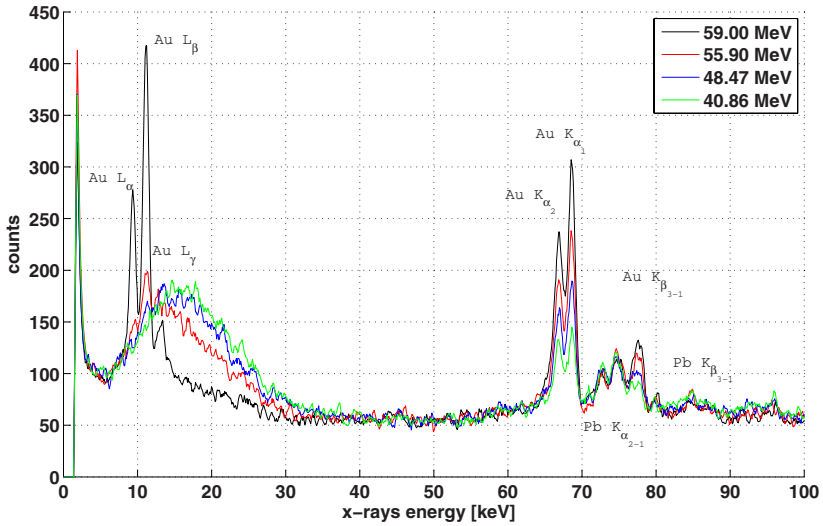

Figure 3. Proton induced x-rays spectra on a gold target at different proton energies. The measured x-ray intensity was corrected for the fluence and the attenuation in the PMMA blocks.

The geometry from the Geant4 example *Hadrontherapy* (Cirrone *et al* 2009) was used. The physics libraries, the step lengths of the simulated interactions and the cut-off parameters were optimized according to Jarlskog and Paganetti (2008).

The physics of PIXE includes the energy loss and scattering of the incident charged particle, atomic shell ionization cross-sections, and atomic transition probabilities and energies. In this study the results discussed by Pia *et al* (2009) were used.

The Monte Carlo results were validated with the experimental results of the experiment described in section 2.6.1. After that the same experimental setup and procedure described in section were simulated on a 3 mm diameter gold marker.

The 15 mm diameter marker covered the entire beam. So the total fluence to the marker was 25 times higher than the fluence delivered to the 3 mm diameter marker, which intersected only a portion of the beam.

3. Results

The PIXE spectra were collected at different positions along the proton penetration curve. As an example, Figure 3 shows the gold spectra in which the characteristic peaks L_α, L_β, L_γ (clearly visible only without any absorber), K_{α_1}, K_{α_2}, K_{β_1} and K_{β_3} are highlighted.

For all our investigations we analysed two peaks to provide greater sensitivity. In practice we used the K_{α_1} and K_{α_2} for both gold (at 68.8 and 66.9 keV) and silver (at 22.16 and 21.99 keV).

The beryllium window of the detector is soldered to the cover with lead and tin. As the lead lines remain when all other sources of lead are removed, this was believed to be the main cause of the lead fluorescence lines contaminating the spectrum.

In order to isolate the useful peaks from the background signal, a region covering both the K_{α_1} and K_{α_2} peaks was selected for analysis. A quadratic least-squares fitting of background non-peak regions was interpolated to give an estimate of the background signal under each peak. The background fit was then subtracted from the measured peak counts in order to

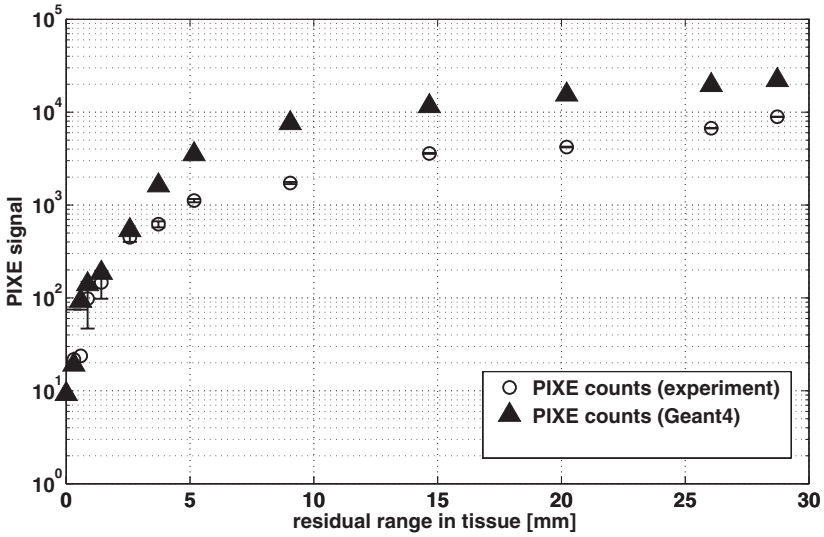

Figure 4. Monte Carlo validation. The two curves represent the number of detected counts with respect to the proton residual ranges in tissue. The triangles refer to simulated results, and circles to the experimentally detected counts. Both sets of data were obtained with pristine Bragg peaks.

isolate the PIXE signal. A Gaussian distribution was fitted to each peak and the area under each distribution was integrated. Finally, all the processed data were corrected for the detector dead-time.

3.1. Range verification with pristine Bragg peak and gold marker

Here the results of our first tests with gold are shown. In figure 4 the number of experimental and simulated detected counts with respect to the residual range in tissue are shown. There is a good agreement between the two sets of data for residual ranges lower than 5 mm. The two curves in differ at higher values of residual range, because of the higher count rates at larger proton energies. This is due to count-rate loss and pulse pile-up in the detector. Pile-up in the amplifier is partly due to scattered protons and neutrons that deposit energy in the detector; this causes spectral distortion (Taguchi *et al* 2010). The dead-time was around 15–20% during these measurements.

The hypothesis that pulse pile-up was due to electrical interference from the cyclotron was excluded during previous experiments at the Douglas cyclotron unit of the Clatterbridge Cancer Centre (UK). During these measurements the beam was extracted from the cyclotron but did not hit either the scatterer or the marker; in this case the spectrum was clear from any background signal.

The validation of the Monte Carlo was necessary in order to simulate the experiment on a clinically sized marker. The x-axis is labelled with the values of the residual range in tissues computed with equation (2).

The depth at which the dose is reduced by 90% (R_0), is in our case equivalent to 25.98 mm of PMMA (z_{PMMA}) and the equivalent depth in eye tissue, z_{tissue} is computed according to:

$$z_{\mathrm{tissue}} = \frac{\rho_{\mathrm{PMMA}}}{\rho_{\mathrm{tissue}}} \frac{S_{\mathrm{PMMA}}}{S_{\mathrm{tissue}}} z_{\mathrm{PMMA}} \tag{3}$$

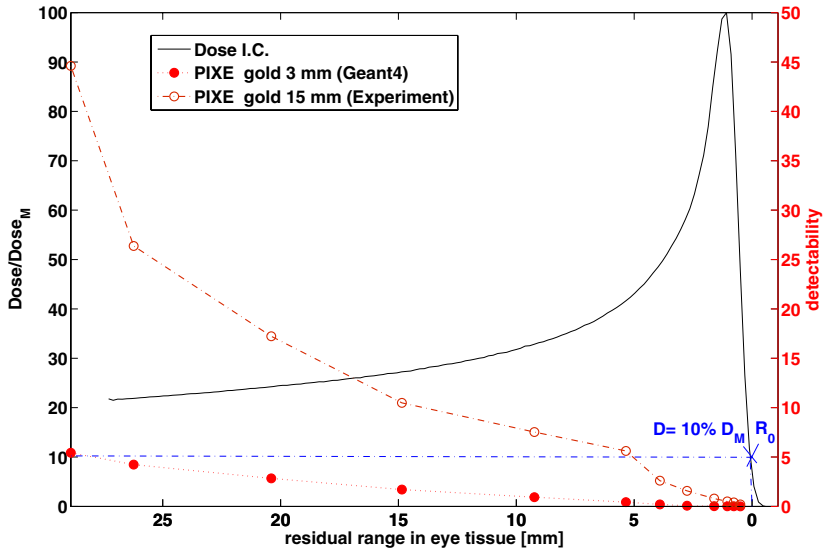

Figure 5. Normalized values (left hand scale) of the dose measured with the plane-parallel advanced Markus Ionization Chamber (type 34 045, PTW, Freiburg, Germany-solid line), with respect to the residual range in eye tissue. The circles (right hand scale) represent the detectability at each marker position for both the 15 mm experimental case (empty circles) and the 3 mm simulated one (solid circles). The range R_0, indicated with the dashed line, was chosen as the depth at which the dose is reduced by 90% of its maximum value.

where we indicated with ρ and S, the density and the stopping power of the two materials, respectively.

In order to measure of capability of the system to distinguish the signal intensity from the random fluctuations of the background signal we define the parameter detectability d,

$$d = \frac{S}{\sigma_B} \tag{4}$$

where S is the peak height of the Gaussian fit to the gold PIXE peak after background subtracted and the background noise σ_B was taken to be the standard deviation of those data points used to calculate the background least-squares fit. A detectability of 1.96 means that the signal is greater than 1.96 σ_B above the background (i.e. $p < 0.05$).

Figure 5 shows the detectability at each marker position for both the 15 mm experimental case (empty circles) and the 3 mm simulated case (solid circles) with respect to the residual range in eye tissue. The dose measured with a plane-parallel advanced Markus Ionization Chamber (type 34 045, PTW, Freiburg, Germany-solid line) (Cirrone *et al* 2004) is also reported as a reference. For both PIXE measurements the detectability is maximum at the entrance of the curve and decreases as we approach the Bragg peak region. The ionization cross-section and thus the number of emitted photons decrease with decreasing proton energies (Denker and Opitz-Coutureau 2004). There is thus a unique correlation between the number of characteristic photons and the residual range (and energy) of the protons that induced them, provided that the proton fluence at the marker is fixed.

The minimum residual range which can be detected with this technique is then defined by the detection limit of the system. More specifically the peak height of the Gaussian fit to the gold PIXE peaks must be at least 1.96 σ_B above the background in order for us to be able

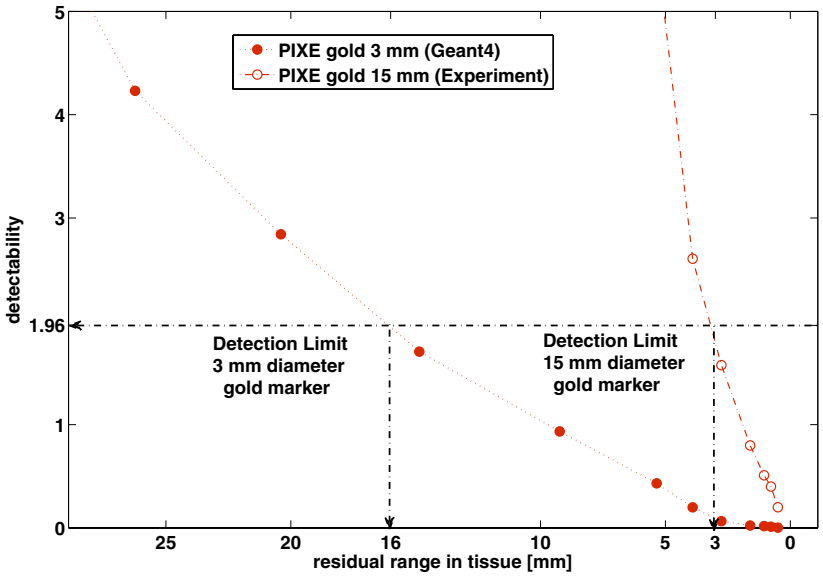

Figure 6. Detection limit for the 15 mm diameter and the 3 mm diameter gold markers. The dose delivered to the marker was 20 GyE. The two curves represent detectability of the two markers with respect to the residual range in tissue of the protons. The black arrows indicate the system detection limit in order to achieve 95% confidence level and the corresponding minimum residual range in tissue which can be detected.

to distinguish the net fluorescence signal from statistical fluctuations with a 95% confidence level (Rousseau 2001). It follows that the detection limit can be determined by finding the residual range at which $d = 1.96$.

Figure 6 shows the detection limit for the 15 mm diameter and the 3 mm diameter gold markers. The diameter of the nozzle was in both cases 15 mm and the equivalent dose to the markers was 20 GyE.

The two curves represent the ratio between the PIXE signal above the background and the standard deviation of the noise. The black arrows indicate the system detection limit ($1.96\ \sigma_B$) and the corresponding values of minimum residual range in tissue which can be detected. The minimum detectable residual range is 3 mm for the 15 mm diameter target and 16 mm for the 3 mm diameter target under clinical conditions. Both values are well above the current uncertainty, making gold unsuitable for this application.

3.2. Silver marker and SOBP

When delivering a SOBP, the beam modulator generates protons with different energies at the same time. So at each position of the marker, the PIXE intensity will be due to the sum of the contributions from the different proton beams at different energies that hit the marker at the same time.

Figure 7 compares the dose depth distribution curve and the detectability of the silver marker at different penetration depths. The x-axis is labelled with the values of the residual range in tissue calculated with equation (2). A detectability equal to 2.1 is achieved when the marker is placed at $z = R_0$ and the residual proton range in tissue is 0. This threshold value corresponds to an equivalent dose to the marker of 1.5 GyE.

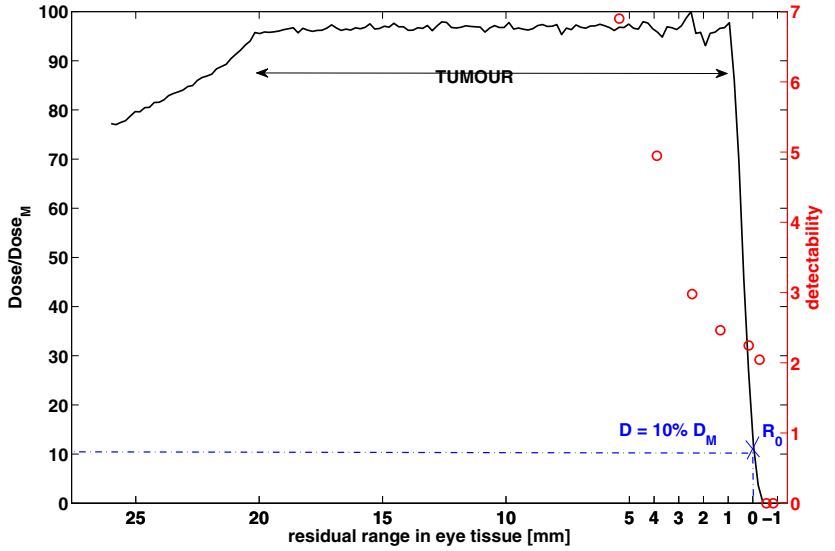

Figure 7. Normalized proton dose distribution curve (left hand scale-black line) and detectability (right hand scale-red circles) of the silver marker with respect to the proton residual range in eye tissue. A detectability of 2.1 is obtained when the marker is placed at a depth equal to the range (R_0).

4. Discussion

In this study we assessed the minimum residual range that is detectable by analysing the number of characteristic x-ray emissions induced on a metal marker during eye proton treatments. Gold (15 mm diameter, 0.2 mm thickness) and silver (5 mm diameter, 0.2 mm thickness) markers were moved along the dose deposition curve of a mono-energetic (59 MeV) proton beam and a fully modulated beam, respectively. The characteristic x-rays from both metals were detected at each depth with a CdTe detector and correlated with the residual proton range in tissue, that is the difference between the initial range of the protons and the marker depth.

The experiment on gold was also modelled in Geant4 and the simulated results were compared with the experimental ones in order to validate the Monte Carlo code. The validation was necessary in order to use the model to assess the feasibility of this technique under clinical conditions.

The experimental results achieved with a gold marker of 15 mm diameter are promising, since a residual range of 3 mm was still detectable with 95% confidence level. Nevertheless by reducing the diameter of the marker down to 3 mm the minimum detectable value of residual range goes up to 16 mm, which is well above the current uncertainty.

An improved residual range resolution is obtained by using a metal with a higher ionization cross-section. This is the case of low atomic number materials (Paul and Sacher 1989). However lower atomic number materials characteristic x-rays have a lower energy, thus experiencing a higher attenuation while passing across the eye. Silver ($Z = 49$) represents a good compromise, since its ionization cross-section at proton energies equal to 3 MeV (2.60 barn) is more than two orders of magnitude greater than gold (1.85×10^{-2} barn) and the energies of its characteristic K_α x-rays are 22.16 and 21.99 keV. This means that 27% of the fluorescence photons are still transmitted across 23 mm of eye tissue (for gold this percentage is 65%).

The second part of the study was then conducted with silver. Results with SOBP show that it is possible to achieve a value of detectability of 2.1 when a 5 mm silver marker is placed at a depth equal to the initial proton range, that is conventionally chosen as the point at which the dose is reduced to 10% of its maximum value.

These values refer to the experimental setup (geometry, detector and dose at the plateau) used in this research study and they do not aim to quantify PIXE ability to resolve range errors. The purpose of this study was to demonstrate the feasibility of the technique rather than fully assess it.

4.1. Factors limiting the detection accuracy and precision

The overall uncertainty in quantitative PIXE analysis is a contribution of the random and systematic errors introduced at each stage of the analysis process.

Random errors are inherent to the PIXE technique and include the counting statistical errors involved in the measurement of both signal and background. They determine the precision of the measurements (i.e. the repeatability of the result).

Systematic errors are mainly introduced by the system and determine the accuracy of PIXE measurement (i.e. the closeness of the measured range error to its true value).

The limits of accuracy and precision from PIXE depend on:

- The metal: ionization cross-section and energy of the emitted x-rays determine the intensity of the emitted signal and its external attenuation, respectively, and are characteristic of the metal atomic number.
- The beam energy: the ionization cross-section also depends on the proton energy and is reduced by 90% when the beam energy goes from 10 to 3 MeV.
- The matrix element: the external attenuation of the emitted x-rays depends on the density of the material they pass through before being detected.

All these limitations can be partially solved by an appropriate choice of the metal. The external attenuation material is fixed in real applications (e.g. eye tissue). The dependence of the PIXE signal on the proton energy cannot be solved and define the real detection limit of the application.

The following detector parameters should be kept into account to reduce systematic errors:

- Energy resolution: a high energy resolution is required to increase the SNR in order to observe the PIXE peak above the background. This will improve the detection limit and increase sensitivity.
- Efficiency of detection at relevant energies: the detecting layer should be of sufficient thickness and made of an appropriate material to maximize efficiency of detection. This will increase the sensitivity of the system.
- Maximum detectable count rate: the detector should be able to operate at high count rates in order to reduce acquisition time, and thus improve sensitivity. Detectors that suffer from pulse pile-up at high count rates degrade the measurement as the spectrum becomes warped due to dead-time losses. With our detector at 2.4 μs the maximum count rate at which spectral distortions and counting losses are avoided is about 70 kcounts s^{-1}. At higher count rates, counts are lost due to pulse pile-up in the detector.
- Dimensions: large detection area is required to increase the solid angle.

The CdTe detector used for this set of measurements have sufficient energy resolution and efficiency. However a detector with higher count rate could allow to increase the intensity of the detected signal of at least half a order of magnitude, at a counting rate comparable with the duration of the treatment.

The main factor that affects accuracy is the reproducibility of the measurement, which was measured to be equal to 19.7% at 46 MeV. This mainly depends on the background noise in the spectrum which is characteristic of the beamline, depends on the geometry and needs to be calibrated at each time. The ideal system should minimize the emissions of secondary x-rays in order not to interfere with our useful signal. Secondaries emitted from the beamline act to worsen the detection limit. Possible dose rate dependence and repeatability of the measurements may be affected by beam intensity instability.

Accuracy improvement can be obtained by applying modification to each component of the experimental system:

- Proton source: in order to achieve a good SNR, the source should be shielded to reduce the gamma and neutron contribution to the useful spectrum. A high SNR will produce a lower error on each data point and so a more accurate linear fit and more tightly constrained 95% confidence bounds.
- Shielding: further improvements to the detector shielding design may be made to improve the accuracy. Reducing the contribution to the background noise due to the proton source or improve the detector shielding would contribute to decrease the background level in the detected spectrum by at least a order of magnitude.
- Geometry and attenuation: error in computation of the attenuation due to PMMA was kept as low as possible during the experimental process. Automatic positioning of the sample and of the detector may be used to give reproducible results. However this is believed to have a minor impact on the quality of the results ($\sim$5%).

5. Conclusions

Based on Monte Carlo simulations and experimental validations, this study establishes that proton induced x-ray emissions (PIXE) from implanted metal markers, could potentially be used to verify in real-time beam range overshoots during eye proton treatments.

A CdTe detector was used to perform some preliminary measurements at the CATANA proton source at INFN-LNS (Italy). PIXE from gold and silver markers was detected at different penetration depths of mono-energetic (59 MeV) and modulated proton beams.

The simulation and the experimental evidence of the amount of produced photons, give evidence that this technique could be potentially useful for clinical purposes. However through the quantitative analysis of the results achieved with our experimental setup we observed that gold is not the most suitable metal due to its low ionization cross-section values. This reduces the ability of the technique to resolve residual ranges $<$16 mm under clinical conditions with our system. The signal is small, due to the strong dependence of the ionization cross-section on the proton energy, and will benefit from a reduction of the improvement of the detection system peak-to-background ratio. Selecting a metal with a higher ionization cross-section ensure to obtain an enhanced signal even at low proton energies. Lower atomic number metals have higher ionization cross-sections values (Paul and Sacher 1989) and silver in particular emits sufficiently high energy photons to be not completely absorbed by the eye. Results with a silver marker of 5 mm diameter show effectively that a detectability of 2.1 is achieved when the marker is placed at the depth at which the delivered dose is reduced to 10% of its maximum value, with the same experimental setup and conditions. In this case the proton residual range is 0 and values of detectability higher than this threshold would be achieved if the range is not correctly estimated and would warn of an unwanted proton dose to the optic nerve. Based on these promising results, silver will be used for future development of this technique. These

are preliminary results which are system dependent and would need further investigations to be confirmed and fully assessed.

Further investigations will focus on assessing what is the minimum dose to the marker, at different proton energies, in order to obtain a reliable signal. If this dose is negligible compared to the prescribed one, our method may effectively be used as pre-treatment 'range check'.

The use of two or more different detectors at different angles could enhance the detectability and improve the accuracy of the system. Integrating the detector and shielding system with the nozzle would increase the solid angle and may improve patient acceptance.

Using an alloy instead of a metal would allow the analysis of characteristic lines at two different energies which would provide extra information that could be used to retrieve proton energy and fluence of the proton beam at the same time and perform dosimetry validation.

Finally our tests were performed in the ideal environment of a single precisely oriented metal marker in a homogeneous PMMA phantom. In a patient the ultimate precision and accuracy of the method will be dominated by more complex heterogeneity effects and the exact determination of the detector position.

Acknowledgments

The authors wish to thank their colleagues from INFN-LNS for their assistance during the collection of the data discussed in this paper. In particular Pablo Cirrone, Francesco Romano, Sara La Rosa, Tiziana Licciardello, Davide D'Urso and Marco Favetta are gratefully acknowledged. The research leading to these results has received funding from the European Union Seventh Framework Programme FP7/2007-2013 under Grant Agreement no. 262010-ENSAR. The EC is not liable for any use that can be made on the information contained herein. We are also grateful for the support of EPSRC (grant EP/F01208X/1).

References

Agostinelli S *et al* 2003 Geant4: simulation toolkit *Nucl. Instrum. Methods Phys. Res.* A **506** 250–303

Amptek 2013 Amptek DPPMCA display and acquisition software http://amptek.com/admca.html

Berger M J 1993 Penetration of proton beams through water: I. Depth-dose distribution, spectra and let distribution *Report NISTIR* 5226*, (Gaithersburg, MD: National Institute of Standards Technology)*

Bortfeld T and Schlegel W 1999 An analytical approximation of depth-dose distributions for therapeutic proton beams *Phys. Med. Biol.* **41** 1331

Cirrone G A P *et al* 2004 A 62-meV proton beam for the treatment of ocular melanoma at laboratori nazionali del sud-infn *IEEE Trans. Nucl. Sci.* **51** 860–5

Cirrone G G *et al* 2009 Hadrontherapy: an open source, geant4-based application for proton-ion therapy studies *IEEE Nucl. Sci. Symp. Conf. Rec.* pp 4186–9

Cuttone G *et al* 2011 Catana protontherapy facility: the state of art of clinical and dosimetric experience *Eur. Phys. J. Plus* **126** 65

Denker A and Opitz-Coutureau J 2004 Proton–induced x-ray emission using 68 meV protons *X-Ray Spectrom.* **33** 61–6

Hocht S *et al* 2004 Proton therapy of uveal melanomas in berlin. 5 years of experience at the Hahn-Meitner institute *Strahlenther. Onkol.* **180** 419–24

IAEA 2006 *Absorbed Dose Determination in External Beam Radiotherapy: an International Code of Practice for Dosimetry Based on Standards of Absorbed Dose to Water (Technical Reports Series* 398*)* (Vienna: International Atomic Energy Agency)

Jarlskog C and Paganetti H 2008 Physics settings for using the Geant4 toolkit in proton therapy *IEEE Trans. Nucl. Sci.* **55** 1018–25

Kacperek A 2009 Protontherapy of eye tumours in the UK: a review of treatment at Clatterbridge *Appl. Radiat. Isot.* **67** 378–86

Kacperek A 2012 *Ion Beam Therapy* vol 320 (Berlin: Springer)

Katsanos A, Aravantinos A and Kallithrakas-Kontos N 1988 Thick target x-ray yield from proton bombardment *X-Ray Spectrom.* **17** 13–6

Kim J, Seo S, Kim K, Kim T, Chung M, Kim K and Yang T 2010 Therapeutic application of metallic nanoparticles combined with particle-induced x-ray emission effect *Nanotechnology* **21** 425102

Lu H M 2008 A point dose for *in vivo* range verification in proton therapy *Phys. Med. Biol.* **53** 1413–24

Meroli S 2012 Energy loss calculator http://meroli.web.cern.ch/meroli/EnergyLossCalculation.html

Munzenrider J E 1999 Proton therapy for uveal melanomas and other eye lesions *Strahlenther. Onkol.* **175** (Suppl. 2) 68–73

Paganetti H 2012 Range uncertainties in proton therapy and the role of Monte Carlo simulation *Phys. Med. Biol.* **57** 99–117

Parodi K and Enghardt W 2000 Potential application of PET in quality assurance of proton therapy *Phys. Med. Biol.* **45** 151–6

Paul H and Sacher J 1989 Fitted empirical reference cross sections for k-shell ionization by protons *At. Data Nucl. Data Tables* **42** 105–56

Pia M G, Weidenspointner G, Augelli M, Quintieri L, Saracco P, Sudhakar M and Zoglauer A 2009 PIXE simulation with Geant4 *IEEE Trans. Nucl. Sci.* **56** 3614–49

Polf J C, Peterson S, Ciangaru G, Gillin M and Beddar S 2009 Prompt gamma-ray emission from biological tissues during proton irradiation: a preliminary study *Phys. Med. Biol.* **54** 731–43

Redus R 2010 Efficiency and attenuation in CdTe detector, amptek application note (an-CdTe-001) http://amptek.com/anczt1.html

Redus R, Pantazis J, Pantazis T, Huber A and Cross B 2009 Characterization of CdTe detectors for quantitative x-ray spectroscopy *IEEE Trans. Nucl. Sci.* **56** 2524–32

Redus R, Pantazis J, Pantazis T, Huber A and Sperry D 2006 Design and performance of the X-123 compact x-ray and gamma-ray spectroscopy system *IEEE Nucl. Sci. Symp. Conf. Rec.* pp 3794–97

Rousseau R M 2001 Detection limit and estimate of uncertainty of analytical XRF results *Rigaku J.* **18** 33–47

Shin D, Yoo S H, Moon S H, Yoon M, Lee S B and Park S Y 2012 Eye tracking and gating system for proton therapy of orbital tumors *Med. Phys.* **39** 4265

Smeets J *et al* 2012 Prompt gamma imaging with a slit camera for real-time range control in proton therapy *Phys. Med. Biol.* **57** 3371–405

Taguchi K, Frey E C, Wang X, Iwanczyk J S and Barber W C 2010 An analytical model of the effects of pulse pile-up on the energy spectrum recorded by energy resolved photon counting x-ray detectors *Med. Phys.* **37** 3957–69

Wilson R 1946 Radiological use of fast protons *Radiology* **47** 487–91